Tracking Snow Avalanches: Integrating Field Observations and Satellite-Derived Indicators

Suvrat Kaushik[1]*, Fatima Karbou[1], Léo Viallon-Galinier[1], Adrien Mauss[2]

[1] Météo-France, CNRS, CNRM, Centre d’Études de la Neige, 38000, Grenoble, France
[2] Météo-France, Centre de Météorologie Spatiale (CMS), 22300, Lannion, France

Keywords: Avalanche mapping, French avalanche database, topography, Sentinel-1, French Alps

Abstract

In this study, we integrated information from the French avalanche database, high-resolution digital elevation models (DEMs), and Sentinel-1 SAR images to model avalanche extents for events occurring across three distinct time periods in three French massifs. The modelled avalanche extents were compared with manually delineated polygons mapped over SAR RGB composites generated using the principles applied in colour-based change-detection algorithms. The comparison revealed strong correspondence between the two independent approaches, with IoU values ranging from 0.42 to 0.47 and F1 scores from 0.58 to 0.63 across the different massifs. We further analyzed the distribution of SAR backscatter values in pre- and post-event images across different zones of the avalanche paths. The results indicated that a fixed 3 dB threshold would most likely be insufficient to capture the full avalanche extent, as some zones showed backscatter increases of less than 3 dB in post-event SAR imagery. As a result, a multi-threshold approach based on different avalanche zones is recommended. Finally, we assessed the potential of Sentinel-2 optical imagery to detect surface changes and characterize the physical behaviour of avalanche-affected paths following intense avalanche events. However, the results were inconsistent, showing the expected trends in one study area but nearly opposite patterns in the other, suggesting that integrating optical data for automated avalanche mapping may not always be reliable.

1. Introduction

Avalanches are among the most devastating natural hazards in mountainous regions, posing a significant threat to infrastructure, ecosystems, transportation networks, tourism, and human life. Accurate avalanche mapping, encompassing the delineation of release areas, flow paths, and runout zones, is crucial for hazard assessment, early warning, land-use planning, protective design, and understanding climate-driven variations in avalanche activity (Eckert and Giacona (2023)). In the densely populated French Alps, where settlements, ski resorts, and transport corridors intersect with steep avalanche-prone terrain, precise mapping is particularly vital for effective risk management and evidence-based policymaking.

Numerous studies have addressed avalanche mapping at regional and massif scales, combining remote sensing, field observations, and statistical or physical modelling. For instance, Bühler et al. (2009) pioneered initial studies using multi-temporal change detection approaches with optical images to detect avalanches, while later works of Nolting et al. (2018) and Kapper et al. (2023) introduced hybrid pipelines integrating Sentinel-1/2, topography, and meteorology for enhanced regional detection. Kneib et al. (2024) applied a semi-automatic approach based on Karas et al. (2022) using Sentinel-1 SAR imagery to map avalanche deposits across the European Alps, Himalayas, and Karakoram, detecting over 16,000 deposits and characterizing their spatio–temporal variability. The same methodology has also been tested by Kaushik et al. (2026) to assess the performance of Sentinel-1 time series for tracking avalanche activity across seven massifs in the French Alps, with results validated against multiple independent avalanche indicators. The influence of topography on avalanche flow has also been extensively studied; for example, Oller et al. (2010) employed the AVAL-1D model to simulate avalanches in the Pyrenees, while Naaim et al. (2004) demonstrated that slope and curvature strongly control flow dynamics and deposition. In addition, deep learning methods have further advanced large-scale mapping, as demonstrated by Hafner et al. (2022), who applied DeepLabV3+ to SPOT 6/7 imagery for avalanche segmentation, achieving results comparable to those of expert delineation. Recent large-scale analyses, such as Hafner et al. (2023), have utilized remote sensing datasets to evaluate the correspondence between observed avalanches and modelled hazard zones. Collectively, these studies illustrate a shift from manual and semi-automated mapping toward fully automated, data-driven frameworks that enable repeatable, large-scale avalanche detection and enhance understanding of regional avalanche dynamics.

In parallel with these scientific efforts, several countries, including France, maintain comprehensive avalanche and snow hazard databases that vary in spatial coverage, temporal depth, completeness, and data accessibility. In the French Alps, the Enquête Permanente sur les Avalanches (EPA) serves as the principal inventory, documenting events across several thousand paths in both the Alps and the Pyrenees. The EPA records detailed event attributes, including event dates, release elevation, runout altitude, deposit characteristics, flow regime, and snow quality, with observations dating back to the early 20th century (Eckert et al. (2010)). This dataset underpins hazard assessment, operational forecasting, and research on avalanche climatology and long-term responses to climate variability.

Despite these advances, avalanche mapping remains constrained by scientific and operational challenges. Steep, remote terrain limits direct observations (Kaushik et al. (2022a,b)), while snow cover, vegetation, and shading obscure past events (Maggioni and Gruber (2003)). The episodic nature of avalanches complicates detection, leading to underreporting of

* Corresponding author

small or infrequent events. Remote sensing techniques face issues such as cloud cover, limited resolution, and difficulties distinguishing avalanche deposits from other snow features (Leinss et al. (2020); Hafner et al. (2021)). Historical inventories also suffer from inconsistencies in path naming, classification, and delineation, while environmental changes, such as vegetation regrowth, erosion, or human modification, can obscure older avalanche evidence. Collectively, these factors hinder the creation of standardized, spatially complete, and reproducible avalanche maps, especially over regional and national scales.

To overcome these limitations, the integration of multi-source data and complementary analytical approaches is increasingly recognized as essential for accurate and comprehensive avalanche mapping. Combining historical inventories, satellite observations, and topographic modelling leverages the strengths of each while mitigating their individual weaknesses. With this in perspective, in this study, information from the French avalanche inventory (EPA) is integrated with high-resolution topography and Sentinel-1 SAR data to refine avalanche boundary delineation across three major French massifs: the Vanoise, Mont-Blanc, and Haute-Bigorre (Pyrenees). The objective is to merge disparate datasets to create accurate representations of avalanche flow paths and boundaries. This approach addresses the limitation of relying solely on one data source, which often lacks spatial detail. The resulting boundaries are compared against manually delineated polygons derived from Sentinel-1 imagery over corresponding spatial and temporal domains.

The paper is structured as follows: Section 2 describes the study area and period; Section 3 outlines the datasets; Section 4 presents the methodology; Section 5 discusses the results; Section 6 interprets and discusses the key findings; and Section 7 concludes with key insights and perspectives for future research.

2. Study Area and time period

The study focuses on three distinct mountainous regions in France: the Mont-Blanc, Vanoise, and Haute-Bigorre massifs, located within the French Alps and the Pyrenees (Figure 1). The Mont-Blanc and Vanoise massifs are located in the Auvergne-Rhône-Alpes region, close to the Italian border, whereas the Haute-Bigorre massif lies further southwest in the Occitanie region, near the boundary with Spain. The Mont-Blanc massif (MBM) is home to the highest peak in Western Europe (4,808 m a.s.l.) and is characterised by steep slopes, deeply incised valleys, and extensive glaciated terrain (Kaushik et al. (2022c)). The total area occupied by MBM is $550km^2$. The Vanoise massif, part of the Graian Alps, is characterized by broad U-shaped valleys, high-elevation plateaus, and several large debris-covered glaciers. The Vanoise massif occupies an area of $1218km^2$ with an average elevation of 2,116 m a.s.l. Located in the central Pyrenees, the Haute-Bigorre massif is the largest massif in our study, with a total area of $1710km^2$, but it has the lowest average elevation of around 2,900 m a.s.l.

The study period was defined by the most significant avalanche episodes documented in recent years across the respective regions, based on the avalanche bulletins published by Météo France and the EPA database. For the MBM, the peak avalanche activity was recorded between January 24 and February 4, 2021. During this period, a total of 88 avalanche events were recorded across the massif, and Météo France issued Avalanche Danger Level 4 (High) multiple times. In the Vanoise, the most active phase was observed from December 25 to January 10, 2018, with a total of 110 individual avalanche events reported in the EPA database. For Haute-Bigorre, the most distinct high-activity period was from January 25 to February 7, 2019, during which EPA reported 105 avalanche events.

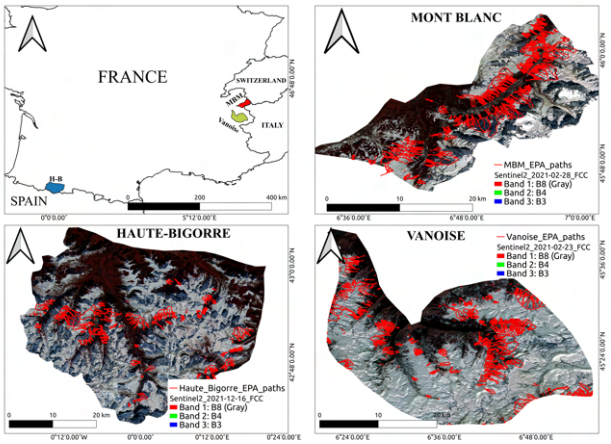

Figure 1. Study area showing the three different massifs. Red polygons highlight the monitored EPA corridors for each area.

3. Datasets used for the study

The study utilizes a range of open-source datasets, including the French national avalanche database (Enquête Permanente sur les Avalanches, EPA), regional avalanche bulletins, Sentinel-1/2 SAR and optical imagery, and a high-resolution Digital Elevation Model (DEM) derived from airborne LiDAR and photogrammetry. As outlined in Section 1, the EPA inventory compiles over a century of observer-based avalanche reports for more than 3000 monitored paths (couloirs or sectors) across the French Alps and Pyrenees. The database is maintained by the French National Research Institute for Agriculture, Food and Environment (INRAE) and is freely accessible at https://www.avalanches.fr/. Each EPA record includes detailed attributes describing the avalanche event and its context; the most important for this study are: (1) Georeferenced shapefiles of all EPA sites, including path contours, main flow lines (thalwegs), and observation or alert altitudes (Figure 2), (2) Temporal information (date and time, with associated uncertainty), (3) Site identifiers (name, administrative location, and code), (4) Elevation data for release and runout zones, or estimated runout distances and (5) Dominant slope aspect for the avalanche event within the monitored path.

For the topographic analysis, the RGE ALTI 5 m Digital Elevation Model (DEM), a high-resolution national product developed and maintained by the Institut national de l’information géographique et forestière (IGN), France’s national mapping agency, was utilized. This DEM provides a continuous representation of mainland France and most overseas territories at resolutions ranging from 1 to 5 meters. It is primarily derived from airborne LiDAR acquisitions (LiDAR HD and LiDAR Lite campaigns) and aerial photogrammetry, complemented by legacy elevation data and field-based corrections. The dataset is openly available under the Etalab Open Data License (v2.0) and can be downloaded from https://geoservices.ign.fr/rgealti. We utilised the Eumetsat-ECMWF Virtual Machine’s computational resources at CMS/Lannion (Centre de météorologie spatiale) to pre-process the Sentinel-1 data using the S1Tiling tool, developed jointly by CNES and CESBIO (see Koleck et

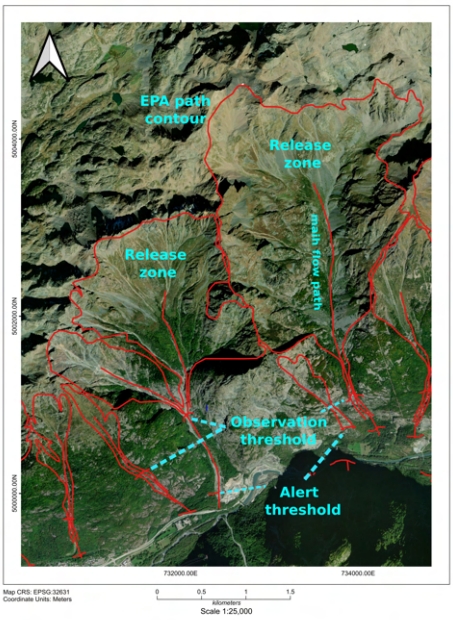

Figure 2. Illustration of a typical EPA path for Vanoise massif. The base image is a 0.5 m aerial orthoimage (freely available to download from: https://geoservices.ign.fr).

al. (2019), and https://github.com/CNES/S1Tiling). This tool facilitates conventional handling of Sentinel-1 Level-1 GRD (Ground Range Detected) data, specifically from the Interferometric WideSwath (IW) mode, by performing orbit correction, thermal noise removal, radiometric calibration, and terrain correction on 100 × 100 km tiles. To suppress speckle noise, co- (VV) and cross-polarized (VH) backscatter channels were averaged using a weighting coefficient based on the ratio of their mean backscatter intensities across the scene:

$$S_{\text{lin}} = \frac{\text{VV}_{\text{lin}} + a\,\text{VH}_{\text{lin}}}{1+a}, a = \frac{\text{mean(VV)}}{\text{mean(VH)}} \quad (1)$$

Averaged images from ascending and descending orbits were subsequently converted to dB, spatially masked, and resampled to match the DEM's coordinate reference system.

Additionally, Sentinel-2 Level-2A Surface Reflectance (SR) optical images were processed and retrieved from the Google Earth Engine (GEE) platform for the study regions where cloud-free acquisitions were available for both pre- and post-event periods. The Sentinel-2 L2A products are atmospherically corrected using the Sen2Cor algorithm and are provided as orthorectified and geometrically refined surface reflectance data.

4. Methodology

4.1 Modelling of avalanche boundaries using information from EPA, topography and Sentinel-1 SAR images

Avalanche boundaries were delineated by integrating information from the EPA avalanche database, high-resolution DEMs, and Sentinel-1 SAR imagery. The workflow comprises three main stages (Figure 3).

Step 1: Filtering EPA avalanche events:
In the first stage, avalanche records from the EPA database (Excel format) and associated geocoded shapefiles (including contours and thalwegs) were filtered according to periods of intense avalanche activity specific to each study area. For instance, events from December 29, 2017, to January 10, 2018, were selected for the Vanoise massif. Matching the `'id_site_epa'` field in the Excel file with the `'ID_Site'` attribute in the shapefile produced a filtered dataset containing only events within the defined temporal window. This step effectively constrained the analysis to validated avalanche polygons corresponding to confirmed events.

Step 2: Determining probable avalanche tracks:
The second stage localized avalanche paths within the filtered polygons by integrating EPA event attributes with topographic information derived from DEM and aspect rasters. Three parameters: maximum release altitude `'altitudes_depart_evt_max'`, minimum deposition altitude `'altitudes_arr_evt_min'`, and dominant aspect `'orientation'` were extracted for each event. These values defined the expected release and deposition points, enabling the algorithm to trace a probable avalanche path downslope following the steepest descent. At each step, the path followed the cell of maximum elevation drop, optionally weighted by the preferred aspect, until the deposition altitude or a local minimum was reached. The resulting polyline represents the estimated avalanche centerline from initiation to deposition.

Step 3: Defining avalanche widths:
In the final stage, avalanche widths were derived using both SAR-based and heuristic approaches. For the physically based method, pre- and post-event S-1 SAR backscatter differences were computed for ascending and descending orbit pairs, reprojected onto the DEM grid, and thresholded at 3 dB to delineate avalanche-affected areas. Based on past research, a post-event backscatter increase of 3–4 dB indicates probable avalanche debris (Leinss et al. (2020)). The algorithm expanded the width outward from the traced centerline within a 100 m radius, including all pixels exceeding the 3 dB threshold in either orbit pair. When backscatter changes were insufficient, a heuristic method estimated half-widths along the centerline based on local slope, assigning narrower widths to steeper slopes and wider ones to gentler terrain. A moving average was applied to smooth the resulting outlines and ensure morphological consistency.

The workflow outputs three primary products: (1) final avalanche polygons representing individual events (referred hereafter as modelled polygons), (2) a filtered EPA shapefile containing validated avalanche polygons within the study period, and (3) a corresponding filtered Excel file listing all relevant events.

4.2 Avalanche extent mapping using the Colour Detection algorithm

To evaluate the accuracy of avalanche boundaries generated by the methodology described in Section 4.1, a reference dataset of avalanche outlines was manually delineated on S-1 SAR imagery. The manual mapping procedure was partly inspired by the automatic colour space segmentation approach proposed by Karas et al. (2022). Pre-processed S-1 GRD VV–VH averaged images served as inputs, with backscatter values clipped to the –25 to –6 dB and normalized to [0, 1]. These normalized images were combined into three-band RGB composites using SAR acquisitions from different dates, where the red (R) and green (G) channels corresponded to consecutive observations

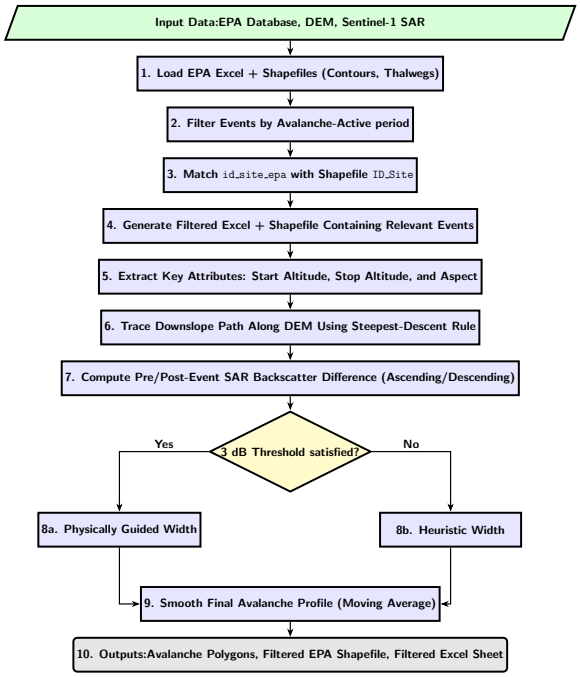

Figure 3. Flowchart illustrating the key steps for generating avalanche boundaries using the methodology described in Section 4.1

and the blue (B) channel represented either (i) a late-summer reference image with minimal snow cover, (ii) a seasonal mean composite, or (iii) the same image used for the red channel. In the resulting composites, avalanche debris typically appeared as bright green pixels, which could be identified either through threshold-based segmentation or manual interpretation. In this study, avalanche boundaries were manually traced over the RGB composites to maintain spatial consistency and avoid fragmented detections often associated with automated thresholding. Mapping was restricted to filtered EPA polygons corresponding to the selected avalanche activity periods, focusing on continuous green patches indicative of avalanche debris. During this process, results from the automated boundary generation method were intentionally withheld to minimize operator bias. The manually delineated avalanche polygons were subsequently used as a reference for comparison with the modelled boundaries.

4.3 Metrics for comparison of results from the modelling and manual mapping approach

Avalanche boundaries derived from both methods were evaluated using standard spatial agreement metrics, including Intersection over Union (IoU), Precision, Recall, and the F1 score (also known as the Dice coefficient). Each metric and its relevance to the comparison are described below.

Intersection over Union (IoU): Quantifies the spatial overlap between two polygon sets and is defined as:

$$\text{IoU} = \frac{\text{Area}(A \cap B)}{\text{Area}(A \cup B)}$$

IoU values range from 0 to 1, where 1 indicates perfect agreement, and 0 denotes no overlap.

Precision: Represents the proportion of the modelled area that correctly overlaps the manually mapped area, defined as:

$$\text{Precision} = \frac{\text{Area}(A \cap B)}{\text{Area}(A)}$$

High precision indicates that most modelled avalanche polygons fall within the manually mapped boundaries, implying minimal over-segmentation.

Recall: Represents the proportion of the reference area captured by the model, given by:

$$\text{Recall} = \frac{\text{Area}(A \cap B)}{\text{Area}(B)}$$

High recall values suggest few false negatives (i.e., most reference avalanches are detected), while low recall indicates missed areas in the modelled results.

F1 Score (Dice Coefficient): The harmonic mean of Precision and Recall, used to balance over- and under-segmentation effects, where A denotes the modelled polygon set and B the manually mapped (reference) polygon set.

4.4 Optical images as an indicator of avalanche activity

For comparison between pre- and post-event Sentinel-2 images for avalanche identification, two primary indicators were analyzed: the change in the Normalized Difference Snow Index, calculated as $(Green - SWIR)/(Green + SWIR)$ (ΔNDSI), and the change in shortwave infrared reflectance ($\Delta B11$). NDSI values range from +1 to -1. ΔNDSI represents the variation in NDSI values between pre- and post-event periods. Avalanche activity typically generates debris that mixes with snow, reducing NDSI values due to lower reflectance in the green and higher reflectance in the SWIR bands. Since clean snow exhibits high NDSI values while debris-covered snow shows lower values, ΔNDSI can effectively indicate avalanche-affected zones when cloud-free imagery is available for both time steps. In contrast, Sentinel-2 Band 11 (SWIR, 1.61 μm) is sensitive to snow grain size and liquid water content, both of which increase SWIR reflectance. Therefore, a positive $\Delta B11$ generally signifies coarser or wetter snow or debris exposure within avalanche deposits. Together, ΔNDSI and $\Delta B11$ provide complementary metrics for identifying and characterizing avalanche activity from freely available optical images.

5. Results

5.1 Comparison of modelled and manually drawn avalanche boundaries

In this section, we present the results of the comparison between avalanche boundaries generated using the modelling approach described in Section 4.1, which integrates information from the EPA inventory, high-resolution DEM, and Sentinel-1 SAR imagery and the manually delineated avalanche outlines produced using the RGB-based colour detection technique described in Section 4.2. Table 1 presents the total number and area of avalanche-affected zones across the three studied French massifs. A noticeable difference is observed between the numbers of modelled and manually delineated polygons, with the latter being fewer due to the exclusion of zones where manual mapping could not be performed reliably. The results also highlight that the highest number of avalanche events was detec-

ted in the Haute-Bigorre massif, but the largest cumulative affected area was in the Vanoise massif, suggesting the occurrence of larger or more extensive avalanches. A comparative assessment between modelled and manually mapped polygons was subsequently conducted for zones common to both datasets, with the results summarized in Table 2. Overall, the modelled and manually mapped avalanche polygons exhibit a satisfactory level of agreement, with both approaches producing spatially comparable outlines. The IoU values range from 0.47 for the Vanoise massif to 0.42 for Haute-Bigorre, indicating a spatial overlap of approximately 42–47 % between corresponding polygons where both datasets are available. High precision values across all regions suggest that most of the modelled avalanche paths correspond well with manually delineated ones, confirming the model's ability to localize avalanche activity within the EPA-defined corridors. Conversely, recall values were consistently lower, suggesting that the manually mapped avalanches extended beyond the modelled outlines, resulting in partial under-segmentation by the model. This trend is also evident in Table 1, where the manually mapped polygons, although fewer in number, exhibit a larger cumulative area than the modelled polygons. The trend can also be seen in Figure 4, where modelled avalanche polygons appear more conservative, typically generated within the manually mapped extents. Despite this conservative tendency, the model effectively constrains the most probable avalanche-affected areas by exploiting EPA, topographic, and SAR-derived information. The F1 scores, which balance precision and recall, ranged between 0.58 and 0.63 across the three study areas, further confirming a consistent and robust correspondence between the two mapping approaches.

	Avalanche count		Total Area (km^2)	
	Modelled	Manual	Modelled	Manual
Vanoise	60	59	2.27	4.03
Haute-Bigorre	99	71	2.27	2.41
Mont-Blanc	33	29	0.68	0.98

Table 1. Statistics for avalanche areas for the three studied massifs

	IoU	Precision	Recall	F1
Vanoise	0.47	0.77	0.51	0.63
Haute-Bigorre	0.42	0.69	0.44	0.58
Mont-Blanc	0.44	0.67	0.46	0.61

Table 2. Performance metrics comparing the modelled avalanche polygons with the manually delineated polygons

5.2 Analysis of SAR backscatter differences along the avalanche flowpaths

In our modelling approach, following previous studies, we adopted a 3 dB increase in backscatter between pre- and post-event SAR image pairs as the indicative threshold for avalanche occurrence. However, the use of such a fixed threshold can lead to systematic underestimation of avalanche extents, particularly for small events or those in which the deposited debris does not substantially enhance surface roughness or, consequently, radar backscatter. To evaluate this limitation, all mapped avalanche polygons were subdivided into three equal sections along the slope: the upper $1/3^{rd}$ corresponding primarily to release zones, the middle $1/3^{rd}$ representing transition zones, and the lower $1/3^{rd}$ encompassing deposition areas (Figure 5).

For each of these zones, backscatter differences between pre- and post-event SAR acquisitions were computed across all

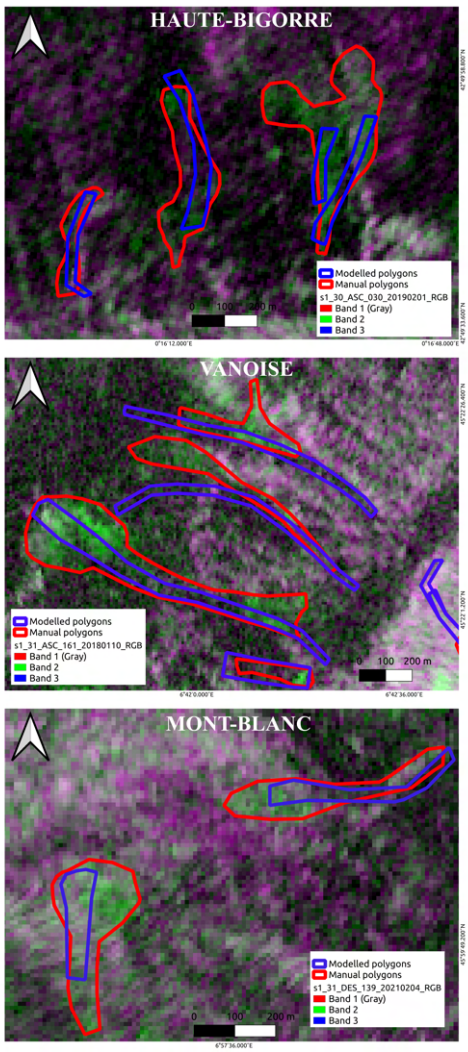

Figure 4. Comparison of the avalanche polygons derived from the modelled and manually mapped approaches across the three studied massifs

avalanches delineated across the three massifs using both the manual and model-based mapping approaches. The results, summarized in Table 3, reveal a consistent trend of backscatter change. The largest mean and median increases in backscatter (in dB) occur within the lower $1/3^{rd}$ part of the avalanche path, corresponding to the debris deposition zone, for both manual and modelled avalanche boundaries. In contrast, the middle zone exhibits the lowest backscatter change values, whereas the upper or release zone generally shows intermediate values, higher than those of the transition zone but lower than those of the deposition zone. These findings have important methodological implications. The spatial heterogeneity of backscatter change within individual avalanche paths suggests that applying a single global threshold (e.g., 3 dB) may fail to accurately capture the full spatial extent of an avalanche, particularly in its release and transition regions. Moreover, our results indicate that the average backscatter difference across all zones is consistently below the conventionally used 3 dB threshold, with lower values observed for polygons generated by the modelling approach than for those manually delineated. This emphasizes the need for adaptive or zone-specific thresholding strategies when delineating avalanche boundaries using SAR data to more accurately represent the entirety of the avalanche path.

This contribution has been peer-reviewed. The double-blind peer-review was conducted on the basis of the full paper.
https://doi.org/10.5194/isprs-annals-XI-3-2026-903-2026 | © Author(s) 2026. CC BY 4.0 License.

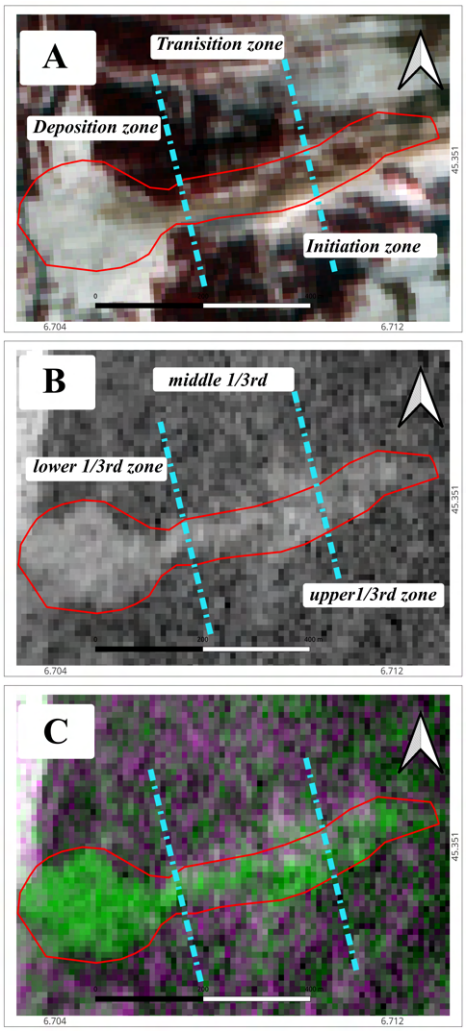

Figure 5. Different avalanche zones as described in Section 5.2. The red polygon represents a manually delineated outline over the SAR-based RGB composite, guided by the green colour. A: Sentinel-2 FCC image, showing an avalanche event; the coarse resolution makes visual mapping challenging. B: Sentinel-1 SAR normalized image highlighting increased backscatter at the avalanche location, C: SAR-based RGB composite.

5.3 Comparison with pre- and post-event Sentinel-2 optical images

As discussed in Section 4.4, similar to changes in SAR backscatter between pre- and post-event acquisitions, variations in optical properties can also be exploited to identify potential avalanche-affected areas. However, such optical changes are not always sufficiently distinct to enable reliable avalanche delineation. To evaluate the effectiveness of optical datasets in this context, cloud-free Sentinel-2 images were processed and analysed for two massifs, Haute-Bigorre and Mont-Blanc. Pre- and post-event cloud-free pairs were unavailable for the Vanoise massif. Two parameters were examined: (i) the change in NDSI values (ΔNDSI) and (ii) the change in SWIR reflectance (ΔB11) between pre- and post-event images over the modelled avalanche polygons. Figure 6 shows the distribution of mean ΔNDSI values across all modelled avalanche polygons for the two study sites. For Haute-Bigorre, ΔNDSI was computed using Sentinel-2 images from January 26, 2019 (pre-event) and February 15, 2019 (post-event), yielding predominantly negative values with a median of -0.493. This indicates a significant decrease in snow cover reflectance following the avalanche period, consistent with expected NDSI behaviour after widespread avalanche activity. In contrast, the Mont-Blanc massif (19 January 2021 pre-event; 8 February 2021 post-event) exhibits an almost opposite trend, with a near-zero median ΔNDSI (-0.006) and a majority of polygons showing increased post-event NDSI values likely due to subsequent snowfall events masking avalanche deposits. Similarly, Figure 7 compares the mean ΔNDSI and ΔB11 (SWIR) values for the same regions. Haute-Bigorre exhibits negative ΔNDSI and positive ΔB11 values, consistent with the presence of wet or debris-rich avalanche deposits. Conversely, Mont-Blanc shows a more variable distribution, making consistent interpretation difficult.

Manually mapped avalanche boundaries			
	Mean	Median	Std
lower $1/3^{rd}$	2.94	2.88	5.80
middle $1/3^{rd}$	1.72	1.65	3.37
upper $1/3^{rd}$	2.07	1.99	3.16
Modelled avalanche boundaries			
	Mean	Median	Std
lower $1/3^{rd}$	2.32	1.86	3.38
middle $1/3^{rd}$	1.65	1.61	3.20
upper $1/3^{rd}$	1.81	1.79	3.28

Table 3. Analysis of SAR backscatter differences (in dB) across the various avalanche zones

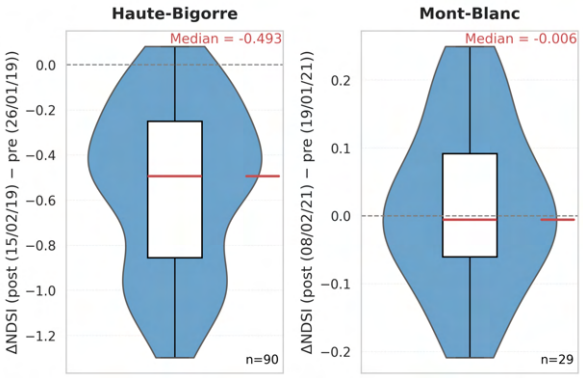

Figure 6. Distribution of mean ΔNDSI values within the modelled avalanche polygons for the Haute-Bigorre and Mont-Blanc massifs

6. Discussion

In Section 5.1, we presented a comparison of avalanche boundaries generated by a modelling framework integrating EPA data, topography, and S-1 SAR imagery with manually delineated polygons derived from SAR RGB composites. The results demonstrated the effectiveness of combining multiple data sources to improve avalanche mapping. The IoU values ranged from 0.42 to 0.47, indicating a reasonable level of agreement between the two approaches. However, higher precision and lower recall values showed that the modelled polygons were generally contained within the manual outlines, reflecting a conservative modelling strategy. In our model, avalanche widths were defined using a strict 3 dB backscatter threshold between pre- and post-event SAR images. As discussed in Section 5.2, this threshold can sometimes be insufficient to capture the full avalanche extent, but it represents the lower limit of backscatter increase typically associated with avalanche activ-

This contribution has been peer-reviewed. The double-blind peer-review was conducted on the basis of the full paper.
https://doi.org/10.5194/isprs-annals-XI-3-2026-903-2026 | © Author(s) 2026. CC BY 4.0 License.

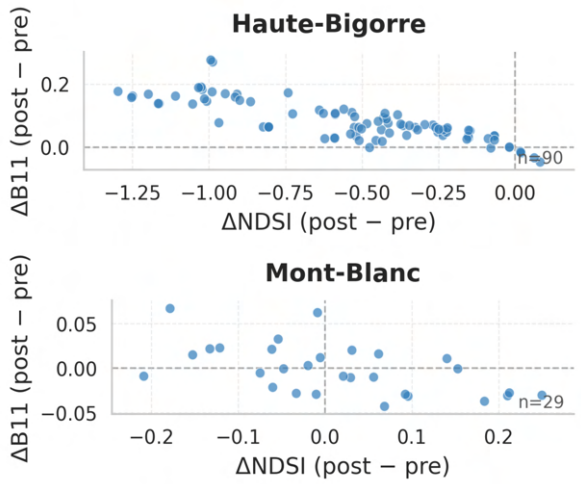

Figure 7. Comparison of the mean ΔNDSI and ΔB11 (SWIR) values for the same two massifs

ity based on previous studies. This conservative value reduces false detections while maintaining realistic widths. For large-scale assessments, the 3 dB threshold remains the most robust; however, for localised analyses focusing on a particular event, testing slightly lower thresholds could better capture the full avalanche extent. The results in Section 5.2 also back this analysis, as we observed significant spatial variability in backscatter differences along different zones of avalanche paths. The largest increases were observed in the lower $1/3^{rd}$ (deposition zone), while smaller changes appeared in the middle $1/3^{rd}$ (transition zone). This pattern is consistent with previous findings (Leinss et al. (2020)), as debris accumulation in the deposition areas significantly increases surface roughness, which in turn increases the backscatter values. The initiation zones also exhibit moderate increases due to the exposure of snow and ice regions from beneath, which increases roughness after the avalanche is released. In contrast, the transition zones show minimal change, as most debris moves downslope, leaving this zone largely unchanged. These variations explain why fixed-threshold SAR differencing approaches often produce patchy detections, capturing the deposition and initiation zones effectively but under-representing transition areas. Consequently, IoU and F1 scores remain low in many previous studies, as the complete avalanche extent is not always identified. Based on these results, we recommend a multi-threshold approach, using different avalanche zones guided by topographic information, to better capture the full extent of the avalanche.

Additionally, in Section 5.3, we evaluated the potential of Sentinel-2 optical imagery for avalanche detection, although these images were not utilized directly in the modelling framework. Despite its spectral properties, which offer certain advantages, the 10 m spatial resolution of S-2 limits reliable manual delineation, even when both pre and post-event cloud-free images are available, and EPA guidance is provided. The availability of S-2 images immediately after avalanche events is also limited, as cloud-free acquisitions often become available only several days or even weeks later, thereby reducing the visibility of avalanche features in post-event imagery. In addition, fresh snowfall events often obscure avalanche-affected areas and increase NDSI values in post-event images, leading to higher NDSI values that are contrary to the expected post-avalanche decrease. As a result, manual mapping was performed using SAR RGB composites over S-2 image pairs. However, in certain areas and events, NDSI and SWIR differencing can provide complementary information to SAR-based methods, as evidenced by results from the Haute-Bigorre massif. However, the results were inconsistent, as seen in the Mont-Blanc massif, where the indices failed to capture any significant changes associated with the reported large-scale avalanche activity. This was likely due to fresh snowfall occurring between the avalanche event and the acquisition of the post-event S-2 image. Therefore, the integration of S-2 information into automated avalanche detection models should be applied cautiously and evaluated on a case-by-case basis, as also recommended previously by Hafner et al. (2021).

7. Conclusions and Perspectives

In this study, we integrated information from multiple freely available sources, including the French avalanche database, open-source high-resolution DEMs, and Sentinel-1 imagery, to model and guide avalanche flow paths. The outputs were compared with independently mapped polygons derived from SAR RGB composites. The results demonstrated that such an integrated modelling approach could accurately delineate avalanche extents, a piece of information that is rarely available. The comparison yielded acceptable IoU, precision, recall, and F1 values, indicating that the modelling results were generally reliable. It is important to note that avalanche extents were delineated using two separate approaches, each with inherent limitations, and should not be regarded as absolute ground truth. Therefore, the comparison between the two methods primarily served to assess how closely each approach captured avalanche extents. A key limitation of the modelling approach is its dependence on the EPA inventory to constrain and guide potential avalanche flow paths, while effectively reducing the search space to highly probable avalanche locations. Consequently, the method, in its current form, is not directly applicable to avalanche events not included in the EPA database. To enhance the scalability and global applicability of this framework, future research should explore more advanced methodologies, such as a modified dynamical systems approach that integrates topographic data with SAR imagery to simulate avalanche paths (James et al. (2024)). Additionally, applying multiple backscatter thresholds according to specific zones along the avalanche path could further improve detection accuracy. Overall, the proposed method, even at this stage, represents a valuable contribution for the rapid delineation of probable avalanche extents in the French Alps, particularly during periods of heightened avalanche activity. In essence, this timely information can enable modellers and authorities to effectively plan and implement disaster mitigation strategies.

8. Data availability

Modelled and manually drawn avalanche shapefiles are available for download from https://doi.org/10.5281/zenodo.17434570.

9. Acknowledgments

The authors would like to acknowledge:

- The financial support provided by the Direction Générale de la Prévention des Risques (DGPR) through the PAPROG (Action Plan for the Prevention of Glacial and Periglacial Risks) initiative.

- The support provided by Centre National d’Études Spatiales (CNES) through the APR SHARE and SnoBelt projects.

References

Bühler, Y., Hüni, A., Christen, M., Meister, R., Kellenberger, T., 2009. Automated detection and mapping of avalanche deposits using airborne optical remote sensing data. *Cold Regions Science and Technology*, 57(2), 99-106.

Eckert, N., Baya, H., Deschatres, M., 2010. Assessing the Response of Snow Avalanche Runout Altitudes to Climate Fluctuations Using Hierarchical Modeling: Application to 61 Winters of Data in France. *Journal of Climate*, 23(12), 3157 - 3180.

Eckert, N., Giacona, F., 2023. Towards a holistic paradigm for long-term snow avalanche risk assessment and mitigation. *Ambio*, 52(4), 711-732. https://doi.org/10.1007/s13280-022-01804-1.

Hafner, E. D., Barton, P., Daudt, R. C., Wegner, J. D., Schindler, K., Bühler, Y., 2022. Automated avalanche mapping from SPOT 6/7 satellite imagery with deep learning: results, evaluation, potential and limitations. *The Cryosphere*, 16(9), 3517–3530. https://tc.copernicus.org/articles/16/3517/2022/.

Hafner, E. D., Techel, F., Daudt, R. C., Wegner, J. D., Schindler, K., Bühler, Y., 2023. Avalanche size estimation and avalanche outline determination by experts: reliability and implications for practice. *Natural Hazards and Earth System Sciences*, 23(8), 2895–2914. https://nhess.copernicus.org/articles/23/2895/2023/.

Hafner, E. D., Techel, F., Leinss, S., Bühler, Y., 2021. Mapping avalanches with satellites – evaluation of performance and completeness. *The Cryosphere*, 15(2), 983–1004. https://tc.copernicus.org/articles/15/983/2021/.

James, G., Karbou, F., Durand, P., 2024. A dynamical system approach to wet snow retrieval using sentinel-1 sar images. *IGARSS 2024 - 2024 IEEE International Geoscience and Remote Sensing Symposium*, 115–120.

Kapper, K. L., Goelles, T., Muckenhuber, S., Trügler, A., Abermann, J., Schlager, B., Gaisberger, C., Eckerstorfer, M., Grahn, J., Malnes, E., Prokop, A., Schöner, W., 2023. Automated snow avalanche monitoring for Austria: State of the art and roadmap for future work. *Frontiers in Remote Sensing*, Volume 4 - 2023.

Karas, A., Karbou, F., Giffard-Roisin, S., Durand, P., Eckert, N., 2022. Automatic Color Detection-Based Method Applied to Sentinel-1 SAR Images for Snow Avalanche Debris Monitoring. *IEEE Transactions on Geoscience and Remote Sensing*, 60, 1-17.

Kaushik, S., Cerino, B., Trouve, E., Karbou, F., Yan, Y., Ravanel, L., Magnin, F., 2022a. Analysis of the Temporal Evolution of Ice Aprons in the Mont-Blanc Massif Using X and C-Band SAR Images. *Frontiers in Remote Sensing*, Volume 3 - 2022.

Kaushik, S., Karbou, F., Eckert, N., Viallon-Galinier, L., Mauss, A., 2026. Can Sentinel-1 reliably provide regional-scale information on avalanche activity. *Cold Regions Science and Technology*, 245, 104822.

Kaushik, S., Leinss, S., Ravanel, L., Trouvé, E., Yan, Y., Magnin, F., 2022b. MONITORING HANGING GLACIER DYNAMICS FROM SAR IMAGES USING CORNER REFLECTORS AND FIELD MEASUREMENTS IN THE MONT-BLANC MASSIF. *ISPRS Annals of the Photogrammetry, Remote Sensing and Spatial Information Sciences*, V-3-2022, 325–332. https://isprs-annals.copernicus.org/articles/V-3-2022/325/2022/.

Kaushik, S., Ravanel, L., Magnin, F., Yan, Y., Trouve, E., Cusicanqui, D., 2022c. Effects of topographic and meteorological parameters on the surface area loss of ice aprons in the Mont Blanc massif (European Alps). *The Cryosphere*, 16(10), 4251–4271. https://tc.copernicus.org/articles/16/4251/2022/.

Kneib, M., Dehecq, A., Brun, F., Karbou, F., Charrier, L., Leinss, S., Wagnon, P., Maussion, F., 2024. Mapping and characterization of avalanches on mountain glaciers with Sentinel-1 satellite imagery. *The Cryosphere*, 18(6), 2809–2830. https://tc.copernicus.org/articles/18/2809/2024/.

Koleck, T., Ballère, M., Marie-Sainte, W., 2019. S1tiling, a multipurpose open source processing chain for sentinel-1 time series. *Proceedings of the Living Planet Symposium, Milan, Italy*, 13–17.

Leinss, S., Wicki, R., Holenstein, S., Baffelli, S., Bühler, Y., 2020. Snow avalanche detection and mapping in multitemporal and multiorbital radar images from TerraSAR-X and Sentinel-1. *Natural Hazards and Earth System Sciences*, 20(6), 1783–1803. https://nhess.copernicus.org/articles/20/1783/2020/.

Maggioni, M., Gruber, U., 2003. The influence of topographic parameters on avalanche release dimension and frequency. *Cold Regions Science and Technology*, 37(3), 407-419. ISSW 2002: International Snow Science Workshop.

Naaim, M., Naaim-Bouvet, F., Faug, T., Bouchet, A., 2004. Dense snow avalanche modeling: flow, erosion, deposition and obstacle effects. *Cold Regions Science and Technology*, 39(2), 193-204. Snow And Avalanches: Papers Presented At The European Geophysical Union Conference, Nice, April 2003. Dedicated To The Avalanche Dynamics Pioneer Dr. B. Salm.

Nolting, S., Marin, C., Steger, S., Schneiderbauer, S., Notarnicola, C., Zebisch, M., 2018. Regional scale statistical mapping of snow avalanche likelihood and its combination with an optical remote sensing based avalanche detection approach – first attempts for the province of south tyrol (italy).

Oller, P., Janeras, M., de Buen, H., Arnó, G., Christen, M., García, C., Martínez, P., 2010. Using AVAL-1D to simulate avalanches in the eastern Pyrenees. *Cold Regions Science and Technology*, 64(2), 190-198. International Snow Science Workshop 2009 Davos.